Date: October 21, 2008
Draft version: 1.2 preliminary
Editors: A. Glazov, M. Klein, J. Kretzschmar, E. Perez, A. Petrukhin
Referees: A. Bunyatyan, V. Chekelian, P. Newman
Deadline for comments: November 3, 2008

A Precision Measurement of the Inclusive *ep* Scattering Cross Section at HERA

H1 Collaboration

Abstract

A precision measurement of the inclusive deep-inelastic e^+p scattering cross section is reported in the region of four-momentum transfer squared, $12\,\mathrm{GeV}^2 \leq Q^2 \leq 150\,\mathrm{GeV}^2$, and Bjorken x, $2 \cdot 10^{-4} \leq x \leq 0.1$. The results are based on data collected by the H1 Collaboration at the ep collider HERA at positron and proton beam energies of $E_e = 27.6$ GeV and $E_p = 920$ GeV, respectively. The data are combined with previously published data, taken at 820 GeV proton beam energy. The accuracy of the combined measurement is typically in the range of $1.5 - 2\%$. A perturbative QCD analysis at NLO is used to determine the parton distributions in the proton based on the final cross section data obtained by H1 using HERA-I data.

To be submitted to *Eur. Phys. J.* **C**

1 Introduction

The electron-proton collider HERA has extended the kinematic range of deep-inelastic lepton-nucleon scattering (DIS), determined by the four-momentum transfer squared, Q^2, and Bjorken x, by two orders of magnitude towards high Q^2 and small x compared to fixed target experiments. This has allowed proton structure to be thoroughly investigated as is vital for the understanding of strong interactions, described by Quantum Chromodynamics (QCD), and of proton-proton interactions at the Large Hadron Collider.

This paper presents the most accurate cross section data for the inclusive neutral current process $e^+p \to e^+X$, measured in the kinematic region $12\,\mathrm{GeV}^2 \le Q^2 \le 150\,\mathrm{GeV}^2$ and $2\cdot 10^{-4} \le x \le 0.1$. The data were taken in the year 2000 with positrons of energy $E_e = 27.6\,\mathrm{GeV}$ and protons of energy $E_p = 920\,\mathrm{GeV}$, corresponding to a centre of mass energy $\sqrt{s} = 319\,\mathrm{GeV}$. Similar data were taken in 1996/97 at $E_p = 820\,\mathrm{GeV}$ [1]. Both data sets are combined here to provide the final H1 measurements for the covered Q^2, x region. The results may be compared with data obtained by the ZEUS Collaboration [2].

The double differential cross section of neutral current DIS, σ_r, in its reduced form and neglecting contributions from Z boson exchange is given by

$$\sigma_r = \frac{Q^4 x}{2\pi\alpha^2[1+(1-y)^2]} \cdot \frac{\mathrm{d}^2\sigma}{\mathrm{d}x dQ^2} = F_2(x,Q^2) - f(y)\cdot F_L(x,Q^2) \tag{1}$$

with the fine structure constant α and $f(y) = y^2/[1+(1-y)^2]$. The inelasticity y is related to Q^2, x and to the centre of mass energy squared, $s = 4E_eE_p$, as $y = Q^2/sx$. This measurement is restricted to the region of inelasticity $y \le 0.6$ and thus its focus is on the proton structure function F_2. A first measurement of the longitudinal structure function F_L at low x and medium Q^2 was recently presented by H1 [3]. The cross section data are used to determine the derivative $(\partial F_2/\partial \ln Q^2)_x$ which provides a sensitive test to the evolution dynamics of partons. An update is also presented of the measurement of the derivative $(\partial \ln F_2/\partial \ln x)_{Q^2}$ which quantifies the rise of $F_2(x,Q^2)$ at fixed Q^2 towards low x [4]. The present paper refers often to methods and detailed explanations given recently in the publication of the lower $Q^2 \le 12\,\mathrm{GeV}^2$ data of H1 [5].

The combination of the present data with lower Q^2 [5] data covers the Q^2 region of DIS from a few GeV^2 to about $100\,\mathrm{GeV}^2$ with unprecedented accuracy at low x. It is therefore used here for a QCD analysis at next-to-leading order (NLO) in order to obtain a new set of parton distribution functions (PDFs) from the inclusive DIS cross section measurements of the H1 experiment alone. The analysis is based on the final results from the HERA-I running period, comprising the present data, the low Q^2 data [5] and the neutral and charged current (NC and CC) data sets at high Q^2 as used in a previous PDF determination of H1 [6].

This letter is organised in three parts: the measurement technique and analysis are presented first, then the cross section data including their combination with the previous data and finally the results of the QCD analysis.

2 Measurement Technique

The present measurement regards the scattering of electrons for medium Q^2 into the backward[1] lead-scintillator calorimeter (SpaCal). This analysis is therefore very similar to that at lower Q^2 recently published in [5] where the measurement techniques have been described in detail. This section is a brief summary providing details only when specific to the larger Q^2 region or the higher level of precision.

2.1 Detector

The H1 detector [7,8] was built and upgraded for the accurate measurement of inelastic ep interactions at HERA. The detector components most relevant to this measurement are the central tracker (CT), the SpaCal and the liquid argon calorimeter (LAr). The central tracker consists of the central jet drift chamber (CJC), the complementary z drift chambers (CIZ and COZ), and the central inner proportional chamber (CIP). It measures transverse momenta of tracks and reconstructs the event vertex for events with tracks from the hadronic final state or the electron within its acceptance. The CIP is also used to provide vertex information from the electron track. The polar angle of the scattered electron is determined by the planar backward drift chamber (BDC) and the vertex position. Complementary tracking information is obtained from the backward silicon tracker (BST). The SpaCal contains electromagnetic and hadronic sections. Its energy resolution for electromagnetic energy depositions is $\delta E/E \simeq 0.07/\sqrt{E/\mathrm{GeV}}$. It also provides a trigger based on the scattered electron energy. The LAr allows the hadronic final state to be reconstructed with an energy resolution of about $\delta E/E \simeq 0.50/\sqrt{E/\mathrm{GeV}}$. The luminosity is determined from the Bethe-Heitler scattering process using a photon calorimeter at $z = -103$ m.

2.2 Kinematic reconstruction

The DIS event kinematics are reconstructed using the angle and energy of the scattered electron and of the hadronic final state. Complementary measurements of Q^2 and y are obtained using the electron and the Σ methods. These employ the measurements of the scattered electron energy E'_e, its polar angle θ_e and the difference between the energy and longitudinal momentum summed over all particles of the hadronic final state, Σ_h. The total $E - P_z$ is obtained adding the electron contribution, $E'_e(1 - \cos\theta_e)$, to Σ_h.

Resolution arguments lead to a preference for these methods in different kinematic regions, which are distinguished by the range of inelasticity, mainly because the measurement accuracy in the electron method, for x and y, diverges as $1/y$. As in previous analyses, the electron method is used at large $y > 0.1$, while the Σ method is used at lower y. The cross section measurement is performed in x, Q^2 bins similar to the previous measurement [1]. For the chosen reconstruction method the values for purity and stability [5] exceed 40% in all analysis bins and are typically well above 50%. For the analysis setup used, the approximate acceptance in the electron scattering angle is $158^\circ < \theta_e < 173^\circ$.

[1]The backward direction is determined by the outgoing electron beam direction. H1 uses a coordinate system with the positive z axis given by the outgoing proton beam direction and the nominal interaction point at $z = 0$.

2.3 Online event selection

The online trigger conditions used in this analysis are based on an energy deposition in the electromagnetic section of the SpaCal (inclusive electron trigger). The analysis requires a minimum energy of 11 GeV, corresponding to y smaller than 0.6. Three different trigger conditions of different energy and radius thresholds are used, which largely overlap in phase space. The combined trigger efficiency is larger than 99.9% as determined from the data with independent triggers.

All triggers contain veto conditions, which reject beam related background. A global inefficiency of 0.5% is determined and corrected for, with an uncertainty of ±0.3%. The inefficiency of the online software filter is determined to be 0.2%, which is applied as a global correction with a systematic uncertainty of half that size.

2.4 Electron and hadronic final state reconstruction

The reconstruction of the scattered electron kinematics is based on the measurement of a deposition of energy, termed cluster, with a limited radius as is characteristic for an electromagnetic shower. This radius, R_{log}, is obtained from the positions of all SpaCal cells belonging to a cluster using a logarithmic energy weighting. In addition, the energy deposition in the hadronic section of the SpaCal behind the electromagnetic cluster, E_{had}, is limited not to exceed 15% of E'_e for additional background suppression. The electron candidate cluster is further required to be associated to a track in the BDC, formed by at least 4 hits from the 8 layers. This ensures an accurate measurement of the polar angle θ_e using the z position of the interaction vertex, z_{vtx}, which is determined with the central track detectors. The polar angle measurement at large angles is cross checked with the BST.

For optimum resolution, the reconstruction of the hadronic final state uses information from the central tracker and the calorimeters LAr and SpaCal [5]. The determination of Σ_h is affected by the presence of noise in the calorimeters. The bias is particularly strong for small $y_h = \Sigma_h/2E_e$. Contributions of noise from the SpaCal and the LAr are removed as described in [5].

2.5 Monte carlo event simulations

Monte Carlo simulations are used to correct for detector acceptance and resolution effects, and for the photoproduction background subtraction. The complete simulation chain and programs have been detailed in [5]. Considering the high level of accuracy required for this analysis an additional sample of elastic QED Compton events is included based on the COMPTON event generator [9]. The cross section measurement is corrected for QED radiation up to order α using HERACLES [10]. The radiative corrections are cross checked with HECTOR [11] to order α. An agreement to better than 0.3% is found in the kinematic range of this measurement.

The MC events are subject to the same reconstruction and analysis procedure as the real data. For consistency, the calibrations of the SpaCal and the LAr, as well as the alignment, are performed for the reconstructed MC events in the same way as for the data. The level of noise in the calorimeters is determined using events from dedicated runs with random triggers which are overlaid on the simulated events. The simulated events are reweighted to match the cross section derived from the QCD fit which is described in section 6.

Description	Cut
Vertex z position	$\lvert z_{\mathrm{vtx}}\rvert < 35\,\mathrm{cm}$
Scattered electron energy	$E'_e > 11\,\mathrm{GeV}$
SpaCal cluster radius	$R_{\log} < 4\,\mathrm{cm}$
BDC validation	$N_{\mathrm{link\ BDC}} \geq 4$
BDC-SpaCal radial match	$\lvert \Delta r_{\mathrm{BDC-SpaCal}}\rvert < 2.5\,\mathrm{cm}$
Hadronic energy fraction	$E_{\mathrm{had}}/E'_e < 0.15$
Transverse momentum balance	$P_{\mathrm{T}}^h/P_{\mathrm{T}}^e > 0.3$
Longitudinal momentum balance	$E - P_z > 35\,\mathrm{GeV}$
QED Compton Rejection	Two back-to-back clusters in SpaCal
Kinematic Range	$Q_e^2 > 10\,\mathrm{GeV}^2$

Table 1: *Event selection criteria used in the analysis.*

3 Data Analysis

The data used for the present measurement were recorded by the H1 Collaboration in the year 2000 and correspond to an integrated luminosity of $22\,\mathrm{pb}^{-1}$. In the following a description of the analysis is given. Further information can be found in [5,12].

3.1 Event selection

An overview of the selection criteria is given in table 1. The event vertex has to be reconstructed either by the central drift chambers or by the CIP. The identification of the scattered electron relies on an energy deposition in the SpaCal and additional matching with the BDC information.

Further selection of events is based on a global momentum balance between the hadronic final state and the electron. Events for which the hadronic final state is poorly reconstructed are rejected by demanding that the total measured hadronic transverse momentum P_{T}^h be at least 30% of the electron transverse momentum P_{T}^e. This efficiently removes migrations from very low y. Events with large initial state radiation are excluded from the measurement by requiring $E - P_z > 35\,\mathrm{GeV}$. The QED Compton process is suppressed using a topological cut against events with back-to-back energy clusters reconstructed in the SpaCal.

3.2 Efficiency determination

The efficiencies of the electron identification requirements (cluster shape, hadronic energy fraction, BDC validation) exceed 99% in most of the phase space. They are everywhere well described by the simulation. The only significant inefficiency is observed for the BDC validation requirement at a radial distance from the beam pipe of $R_{BDC} \sim 25\,\mathrm{cm}$ where the geometry of the BDC drift cells changes. A detailed map of this inefficiency is obtained using electron candidates validated by the BST, studied as a function of R_{BDC} and the azimuthal angle of the scattered electron. This inefficiency is included in the simulation, and an additional 0.5% local systematic uncertainty is added to the measurement error.

The efficiency to reconstruct the event vertex is determined using events independently reconstructed by the BST. It is close to 100% for all but a few bins at $Q^2 < 20\,\mathrm{GeV}^2$ and $y < 0.03$, where it drops to about $75-95\%$. The vertex efficiency is described by the simulation accurately to 0.3% for $y > 0.01$. For lower y the description is accurate to about 1%, which is covered by an additional uncorrelated uncertainty in the corresponding bins.

3.3 Alignment and calibration

The alignment of the H1 detector starts from the internal adjustment of the central tracker and proceeds with the backward detectors, BDC, SpaCal and BST. The alignment of the BDC is performed using tracks of the electron candidates reconstructed in the central tracker with high accuracy. The SpaCal position is adjusted based on the electron tracks measured in the BDC. Finally the BST is aligned using events with a well reconstructed central vertex and the electron track measured in the BDC. The resulting agreement of the polar angle measurement is better than 0.2 mrad which is taken as a systematic uncertainty for the cross section measurement.

The calibration of the electromagnetic scale of the SpaCal calorimeter corrects for differences in the gain factors of individual SpaCal cells, for local non-uniformities at sub-cell level and for global non-linearity. The calibration is based mainly on the electron candidates at low y. There the kinematics can be reliably reconstructed using a double angle reconstruction method as described in [5], which employs only polar angle information of the hadronic final state, the scattered electron, and the electron beam energy. The non-linearity of the energy response is determined using a sample of $\pi^0 \to \gamma\gamma$ events. The energy scale is then checked using quasi-elastically produced J/ψ particles decaying to e^+e^- and QED Compton events, $ep \to ep\gamma$, where the scattered electron and photon are both reconstructed in the SpaCal.

The results of all electromagnetic calibration studies are summarised in figure 1. The scale at the beam energy is determined by the double angle calibration and at $E = 2\,\mathrm{GeV}$ by the π^0 calibration. The uncertainties of these two procedures determine the relative data-to-simulation scale uncertainty as a function of energy as shown in figure 1. Both the J/ψ and the QEDC energy scale determination at intermediate energies are compatible with the uncertainty band. The measured and simulated scattered electron energy distributions, with uncertainty bands attached to the simulated E'_e distributions, are compared in figure 2a). As for the polar angle, figure 2b), the data are well described by the simulations. The uncertainty for the energy scale is derived from two contributions: a global 0.2% for the double angle calibration and a part resulting from the low energy adjustment of the π^0 mass, which is 1% at $E = 2\,\mathrm{GeV}$ linearly decreasing to zero at $E = 27.6\,\mathrm{GeV}$.

The calibration of the calorimeters employed for the hadronic final state energy measurement is based on kinematic constraints relating the scattered electron to the hadronic final state. For the calibration of the LAr calorimeter, the conservation of the total transverse momentum P_T is used. The hadronic SpaCal calibration utilises the conservation of $E - P_z$.

The transverse momentum balance between the scattered electron and the calibrated hadronic final state is studied as a function of various variables, such as P_T^e, the polar angle θ_h of the hadronic final state and y_Σ. At the lowest $y \sim 0.005$ considered in the measurement, the hadronic final state is produced at small polar angles, and it partially escapes the forward calorimeter acceptance. The systematic uncertainty of the hadronic energy scale is extrapolated linearly in $\log y$, from 10% at $y_\Sigma = 10^{-3}$ to 2% at $y_\Sigma = 10^{-2}$. It is taken as 2% for larger y_Σ. Figure 2c) shows the overall $P_{\rm T}$ balance for the standard analysis selection. The vertical line at $P_t^h/P_t^e = 0.3$ indicates the analysis cut value. For larger P_t^h/P_t^e, the distribution for the data lies inside a band given by the simulation for which the LAr hadronic scale is varied as described above. An enlarged discrepancy between the data and the simulation is observed in the region of $y_\Sigma < 10^{-2}$, where a variation of the analysis selection on $P_{\rm T}^h/P_{\rm T}^e$ is used to estimate an additional uncorrelated cross section uncertainty of 2% for bins in this region.

For $y \lesssim 0.03$, even a small fake energy measurement in the LAr can strongly affect the determination of y_h. Therefore, a dedicated topological noise finder is used to identify and subtract LAr noise. The fraction of hadronic energy attributed to noise is described by the simulation within 15% which is taken as a systematic uncertainty.

For large values of y, the contribution of the SpaCal to the total $E - P_z$ becomes larger than the combined contribution of the LAr calorimeter and tracks and thus $E - P_z$ provides a good calibration tool for the hadronic final state measurement in the SpaCal. A study at $y \sim 0.5$ shows that the hadronic energy measurement in the SpaCal is described by the simulation to 0.3 GeV. Figure 2d) shows the $E - P_z$ distribution for the data and the simulation. The simulation reproduces the data within the combined calibration uncertainties.

3.4 Background

A small source of background for this analysis arises from very low Q^2 photoproduction events, in which the scattered electron escapes detection in the backward beam pipe while a particle from the hadronic final state mimics the electron. For a fraction of photoproduction events the scattered electron is detected by the electron tagger of the luminosity system. The acceptance covers the range $0.3 < y < 0.6$. The photoproduction background MC (PHOJET) is normalised globally based on tagged events applying all selection criteria but the $E - P_z$ cut. The systematic uncertainty on the background normalisation is taken to be ±15%, based on extensive studies performed in [5]. The resulting correction at the highest $y \sim 0.5$ considered here, is typically 5% only, corresponding to an uncertainty of less than 1%. Potential background from non-ep interactions is studied using non-colliding bunches and found to be negligible.

3.5 Luminosity determination

The luminosity measurement is based on Bethe-Heitler events detected using the photon detector. The accuracy of the measurement requires a good understanding of the beam optics, of the photon detector acceptance and of its variation with beam conditions.

The time structure of the ep interaction is characterised by the main proton bunch accompanied by satellite bunches. Two such bunches are located at about ±70 cm distance from the mean vertex position. The photon detector cannot distinguish interactions at the nominal vertex position from satellite bunch interactions. The luminosity measurement is therefore corrected for satellite bunch contributions which are determined independently. Also electron beam - gas interactions are corrected for using non-colliding electron bunches.

Correlated error	
Source	**Uncertainty**
E'_e scale uncertainty	0.2%
E'_e linearity uncertainty	1% at 2 GeV to 0% at 27.6 GeV linearly
θ_e uncertainty	0.2 mrad
LAr scale uncertainty	2% for $y > 0.01$
	increasing linearly in $\log y$ to 10% at $y = 0.001$
LAr noise contribution to $E - P_z$	15%
SpaCal hadronic scale	0.3 GeV
γp background normalisation	15%
Luminosity and other global uncertainties	1.2%
Uncorrelated error	
Source	**Uncertainty**
BDC efficiency	0.5%
Vertex efficiency	0.3%
Radiative corrections	0.3%
Additional uncertainty for bins with $y \leq 0.01$	2.0%

Table 2: *Summary of the systematic uncertainties. For the correlated error sources, the uncertainties are given in terms of the uncertainty of the corresponding source. For the uncorrelated error sources, the uncertainties are quoted in terms of the effect on the measured cross section directly.*

3.6 Summary of systematic uncertainties

The systematic uncertainties are classified into two groups, bin to bin correlated and uncorrelated systematic errors. They are summarised in table 2. The electromagnetic and hadronic energy scales, the electron scattering angle, calorimeter noise, background subtraction and normalisation are all considered to be correlated sources of uncertainty. The uncorrelated errors arise from various efficiencies and the radiative corrections. For most of the analysis phase space none of the sources of systematic uncertainty dominates the result. For very low $y < 0.01$, many uncertainties increase strongly, as the reconstruction efficiency drops rapidly and the modelling of the hadronic final state suffers from increased losses in the forward direction.

The uncertainty on the global normalisation of the measurement is determined mostly from the luminosity measurement, which is known to 1.1% for this data period. The additional corrections discussed in section 2.3 increase the overall normalisation uncertainty to 1.2%.

4 DIS Cross Section Results

The simulation of the measurement can be verified by comparing experimental and simulated distributions. The approximate kinematic range of the measurement is selected requiring $y_e < 0.6$ and $y_\Sigma > 0.005$. Figure 3(a-d) shows the x, Q^2 distributions for the two kinematic reconstruction methods, e and Σ. The DIS MC cross section prediction is reweighted to the QCD fit discussed in section 6. The distributions are normalised to the luminosity, adjusting the MC prediction for the 920 GeV data shown here for a small overall normalisation shift introduced by the cross section averaging procedure and the QCD fit, see tables 3 and 5. A very good overall agreement is obtained in the description of the data by the simulation.

The stability of the cross section measurement is tested with a set of dedicated cross checks. The robustness of the cross section measurement for a chosen reconstruction method is studied by splitting the data into two approximately equal subsamples and comparing these subsamples to each other. For example, the data are compared as measured with the upper and the lower half of the SpaCal, for negative and positive z_{vtx} positions, and dividing the sample into early and late data taking periods. These tests are sensitive to local efficiency problems, energy miscalibrations and the stability of the luminosity measurement, for example.

A particularly interesting test is the comparison of the cross section measurement performed with the electron and Σ methods, which have different sensitivities to systematic error sources. The results shown in figure 4 demonstrate very good agreement taking the correlated uncertainties into account.

For the cross section data reported in tables **??** and **??** the method with the smaller total uncertainty is chosen in each bin, which results in a transition between the two methods near $y = 0.1$. The tables show the statistical, uncorrelated and the various correlated error contributions.

The result of this analysis represents the most accurate measurement of the inclusive DIS cross section in this kinematic range. It improves the uncertainties by up to a factor of two with respect to previously published results by ZEUS [2] and by H1 [1].

5 Combination of 820 and 920 GeV Data

The present measurement is based on data taken with 920 GeV proton beam energy. A similar data set was obtained in 1996/97 at 820 GeV and published in [1]. A comparison of the two data sets revealed a significant deviation which required a dedicated study as described below. The combination of the two data sets, after correction of the 820 GeV data, provides the final H1 cross section measurements at medium Q^2 from the HERA-I data taking period, extending from 1992 to 2000.

5.1 Correction of the 820 GeV data

For the analysis of the 820 GeV data an older version of the simulation program DJANGO was used. It was found, that this version leads to biased results when a weighting procedure is applied for all $Q^2 < Q^2_w$, where Q^2_w can be chosen by the user. If the weighting is disabled, the simulation results agree to better than 0.5% with the HECTOR calculation, as had been studied in [1]. To improve the statistical accuracy, however, the simulated events in [1] were taken from a weighted event generation, with $Q^2_w = 50\,\mathrm{GeV}^2$. The Q^2 depend bias introduced by the weighting is here corrected for by using a factor, c_{DJ}, defined as

$$c_{DJ}(Q^2) = \frac{N^{weighted}_{MC}(Q^2)}{N_{MC}(Q^2)} . \tag{2}$$

Here $N_{MC}(Q^2)$ and $N_{MC}^{weighted}(Q^2)$ are the sums of weights of events generated for a given Q^2 bin in unweighted and weighted mode, respectively. The correction factor shown in figure 5 is empirically parametrised by the following function

$$c_{DJ}(Q^2) = \begin{cases} c_0 & \text{for } Q^2 > Q^2_w \\ c_0 + c_1 \cdot \log_{10}(Q^2/Q^2_w) & \text{for } Q^2 \leq Q^2_w \end{cases}, \tag{3}$$

with $c_0 = 1.027$ and $c_1 = 0.0352$. This correction procedure introduces an additional cross section uncertainty of 0.5% uncorrelated from bin to bin.

The 1996/97 data were completely reanalysed within the framework of the present analysis. The luminosity determination was improved, resulting in an additional normalisation shift by +0.5%, corresponding to one third of a standard deviation of the quoted normalisation uncertainty. No further significant deviation was observed between the previous and the cross check analysis.

Tables **??** and **??** present the 1996/97 data, the so called sample A from [1], corrected for the Q^2 weighting and the small luminosity shift. These tables therefore replace the previous data for $Q^2 \geq 12\,\mathrm{GeV}^2$. The measurements of F_2 for $y < 0.6$ are extracted from the corrected cross sections correcting for the F_L influence, as described in section 5.3. The sample B in [1], extending to lower Q^2 values, was not affected by the MC weighting problem and has been combined with further H1 data as described in [5].

5.2 Combined cross sections

The corrected 820 GeV data and the present 920 GeV data are combined to determine the final H1 data set at medium Q^2. The combination of the data sets is based on the prescription introduced in [13] and developed further in [5]. The combination uses the reduced cross section data and consistently treats the correlated and uncorrelated uncertainty information, which is given in the tables **??**-**??**. The data are combined for the larger x region, defined as in [5] by $y < 0.35$, but kept as independent data at higher y where the reduced cross section significantly depends on the centre of mass energy via the F_L term. Small differences in the binning are adjusted by floating points to the same x values.

In the combination of the two data sets, assumptions have to be made about the relation between systematic uncertainty sources, which may not be fully independent between the different analyses of the 1996/97 and 2000 data. Reasons for correlations between data sets are the similarity in the calibration procedure and the detector setup, which must be balanced against uncorrelated effects such as variations with time, beam conditions and changes in the analysis procedure. To estimate the sensitivity of the averaged result to the correlation assumptions, the average of the 1996/97 and 2000 data obtained by considering all systematic error sources to be uncorrelated is compared with all other possible assumptions, in which each source is taken to be either correlated or uncorrelated. The observed variation of the average cross sections is typically at the per mill level, which is negligible compared with the total uncertainty. The variation of the total uncertainties never exceeds 10% of the uncertainty. The assumption that the systematic uncertainties of the two data sets are uncorrelated yields the largest uncertainty.

Table 3: *Shifts of the systematic uncertainties determined based on the combination of the 1996/97 data at 820 GeV and the 2000 data at 920 GeV proton beam energy. The value for each shift is given in units of the original uncertainty σ.*

Systematic Source	**Shift in σ**	
	1996/97	2000
E'_e scale	0.72	0.50
E'_e low energy scale	—	−0.38
θ_e	−0.47	0.08
LAr scale	−0.86	−0.12
LAr noise	−0.22	0.05
SpaCal hadronic scale	—	0.35
γp background	0.11	−0.11
Luminosity	0.64	−0.48

Based on this study, it is assumed that there are no correlations between the error sources of the 1996/97 and 2000 data in the combination procedure.

The 1996/97 and 2000 data sets are fully consistent, as determined in the averaging procedure, with $\chi^2_{tot}/\,\mathrm{ndf} = 51.0/61$. The shifts of the central values of the systematic uncertainties are given in table 3. It is remarkable that none of the absolute values of the shifts exceeds one standard deviation. Since the new data are more precise than the previous data, the average tends to favour them.

The resulting measurement of the reduced ep scattering cross section and its uncertainties are listed in tables **??** and **??**. The correlated uncertainties are given as 14 new sources, δ_i, after diagonalisation of the error matrix as is explained in [5]. These data represent the most precise inclusive cross section measurement by the H1 experiment in the medium Q^2 region with total uncertainties in most of the phase space close to 1%.

5.3 F_2 and its derivatives

The cross section data are used to extract F_2 for $y < 0.6$ using a QCD calculation of $R = F_L/(F_2 - F_L)$ as is quoted in the cross section tables. Figure 6 shows the proton structure function F_2 together with H1 data from lower [5] and higher Q^2 [6]. The data are well described by the NLO QCD fit introduced below. The rise of F_2 towards low x is thus established at a much improved accuracy compared to the initial observation [14], and there is no indication for a saturation of this behaviour in the Q^2 region of study.

Figure 7 shows the measurement of the structure function F_2 at fixed values of x as a function of Q^2. The strong rise with Q^2 at low x is a consequence of the large gluon density in this region, see below. The data are well described by the QCD fit. At the largest x value covered by the data presented here, the structure function becomes almost independent of Q^2 as the result of a compensation of quark and gluon contributions to the $\ln Q^2$ derivative of F_2.

The DGLAP evolution equations determine the derivative $(\partial F_2/\partial \ln Q^2)_x$ taken at fixed x. The measurement of this derivative has long been recognised as a powerful constraint on the gluon distribution xg and the strong coupling constant α_s [15]. A study of $(\partial F_2/\partial \ln Q^2)_x$ at low x was presented previously by the H1 Collaboration [1]. The method described there has been used to determine this derivative using the new, combined F_2 data set, including the low Q^2 data [5]. The results are shown in figure 8 for different x as a function of Q^2. At low x, the shape of $(\partial F_2/\partial \ln Q^2)_x$ reflects the behaviour of the gluon distribution. The dependence of the derivative on Q^2 is well reproduced by the QCD fit.

The rise of the structure function $F_2(x, Q^2)$ towards low x may be quantified by the derivative $\lambda = -(\partial \ln F_2/\partial \ln x)_{Q^2}$ which is shown in figure 9. The result is more accurate than the previous measurement [4] and extends it to lower Q^2. Within the uncertainty of the data, the derivative is constant at small $x < 0.01$, i.e. F_2 for fixed Q^2 is consistent with a power law $F_2 \propto x^{-\lambda}$. Small departures from this behaviour, as inherent to the QCD fit, cannot be excluded either. The value of λ increases from about 0.1 to 0.3 in the covered Q^2 region, from about 1 to 100 GeV^2. Data from [5] allow this measurement to be extended to Q^2 values too low for a DGLAP fit to be valid.

6 QCD Analysis

The neutral current cross section measurements presented here, together with the measurements at lower Q^2 [5] and the NC and CC data at higher Q^2 previously published [6,16,17], provide an accurate H1 data set for the determination of the parton density functions of the proton. A new QCD analysis, termed H1PDF-HERA-I, is performed which supersedes the previous H1 PDF 2000 fit [6], as it uses the more accurate new data. It also uses a general variable flavour number scheme (VFNS) treatment [18] of the heavy quarks, unlike the former fit which used a zero mass variable flavour number scheme ("massless" scheme).

6.1 Framework and settings

The QCD analysis uses a set of parton densities, the gluon xg, the valence quarks, xu_v and xd_v, and the combined anti-up type and anti-down type quarks, $x\bar{U} = x\bar{u} + x\bar{c}$ and $x\bar{D} = x\bar{d} + x\bar{s} + x\bar{b}$, all of which are parameterised[2] at a starting scale Q_0^2. The densities are evolved using the DGLAP evolution equations, and an adjustment of the parton distribution parameters is performed to best fit the measured cross sections.

The analysis is performed at the NLO within the $\overline{MS}$ renormalisation scheme. The program QCDNUM [19] is used to solve the evolution equations. From the evolved parton distributions, the structure functions are calculated in the VFNS scheme [18,20]. The factorisation and renormalisation scales are both set to Q^2. A χ^2 function as defined in [1] is minimised using the MINUIT package. The correlations between data points caused by systematic uncertainties are taken into account as in [6], following the numerical method presented in [21,22]. The

[2]Note that the previous H1 PDF 2000 fit used a very similar decomposition of the quark flavours. The difference was that instead of the valence quark distributions, xu_v and xd_v, the combined up and down quark distributions, xU and xD, were used. These determine $xu_v = xU - x\bar{U}$ and $xd_v = xD - x\bar{D}$ assuming symmetry between the sea quarks and antiquarks for each flavour.

correlations between the systematic error sources of the different high Q^2 data sets are treated as described in [6], table 2. The error sources of the data presented here and of the lower Q^2 data [5] are all taken as not correlated to any other source, except for the theoretical 0.5% luminosity uncertainty, which is common to all H1 cross section measurements.

Following [23], the masses of the charm and beauty quarks are set to $m_c = 1.4\,\mathrm{GeV}$ and $m_b = 4.75\,\mathrm{GeV}$, respectively. The value of the strong coupling constant is taken to be $\alpha_s(M_Z^2) = 0.1176$ [24]. The starting scale Q_0^2 is chosen to be slightly below the charm threshold, $Q_0^2 = 1.9\,\mathrm{GeV}^2$. Hence, $x\bar{U}(x) = x\bar{u}(x)$ and $x\bar{D}(x) = x\bar{d}(x) + x\bar{s}(x)$ at the starting scale. The strange quark density, $x\bar{s}(x) = f_s x\bar{D}(x)$, is taken to be a constant fraction, $f_s = 0.33$, of $x\bar{D}$ at the starting scale. A cut $Q^2 > Q^2_{min} = 3.5\,\mathrm{GeV}^2$ is applied in order to ensure that the data used in the fit correspond to a kinematic domain where perturbative QCD can considered to be valid. Variations around these central values are taken into account as model uncertainties.

6.2 Parameterisation

The initial parton distributions xP are parameterised at Q_0^2 using the general form

$$xP(x) = A_P x^{B_P} (1-x)^{C_P} \left[1 + D_P x + E_P x^2\right] . \tag{4}$$

As in [6], the specific choice of the parameterisations is obtained from saturation of the χ^2: a parameter D or E is considered only when its introduction significantly improves the χ^2. This procedure, for $Q_0^2 = 1.9\,\mathrm{GeV}^2$, leads to the following choice:

$$\begin{aligned}
xg(x) &= A_g x^{B_g} (1-x)^{C_g}, & (5)\\
xu_v(x) &= A_{u_v} x^{B_{u_v}} (1-x)^{C_{u_v}} \left[1 + E_{u_v} x^2\right], & (6)\\
xd_v(x) &= A_{d_v} x^{B_{d_v}} (1-x)^{C_{d_v}}, & (7)\\
x\bar{U}(x) &= A_{\bar{U}} x^{B_{\bar{U}}} (1-x)^{C_{\bar{U}}}, & (8)\\
x\bar{D}(x) &= A_{\bar{D}} x^{B_{\bar{D}}} (1-x)^{C_{\bar{D}}}. & (9)
\end{aligned}$$

Removing the E parameter in the parameterisation of $xu_v(x)$ degrades the χ^2 by 8 units. The normalisation parameters A_{u_v} and A_{d_v} are not fit but obtained from the other parameters via the quark counting rules. Since the existing data have a limited sensitivity to the behaviour of the valence quark distributions at low x, it is assumed that $B_{u_v} = B_{d_v}$. Similarly, the behaviour of the up and down anti-quarks at low x is assumed to be governed by the same power, $B_{\bar{U}} = B_{\bar{D}}$. As in [6], the normalisations of the $\bar{U}$ and $\bar{D}$ distributions are related by $A_{\bar{U}} = A_{\bar{D}}(1 - f_s)$ which corresponds to the usual assumption that $\bar{d}/\bar{u} \to 1$ as $x \to 0$. Finally, the normalisation A_g of the gluon distribution is derived from the momentum sum rule. The total number of free parameters is thus equal to ten.

6.3 Fit results

The fit has a χ^2 of 589 for 645 degrees of freedom. The χ^2 value for each data set is given in table 4, together with the optimised relative normalisations as determined from the fit. The

data set		data points	χ^2_{unc}	normalisation
low Q^2	[5]	59	56.1	-0.1%
medium Q^2	this measurement	99	89.3	-1.4%
e^+p NC high Q^2, 94 – 97	[16]	130	89.7	$+0.1\%$
e^+p CC high Q^2, 94 – 97	[16]	25	19.8	$+0.1\%$
e^-p NC high Q^2, 98 – 99	[17]	139	115.8	$+0.9\%$
e^-p CC high Q^2, 98 – 99	[17]	28	17.1	$+0.9\%$
e^+p NC high Q^2, 99 – 00	[6]	147	143.9	$+0.7\%$
e^+p CC high Q^2, 99 – 00	[6]	28	28.1	$+0.7\%$

Table 4: *For each data set used in the H1PDF-HERA-I fit, the number of data points is shown, along with the χ^2 contribution determined using the uncorrelated errors only (χ^2_{unc}), and the optimised normalisation of the data set as determined by the fit.*

fit does not require to shift significantly the normalisation of any data set. Also no significant tension is observed between the fit results and the systematic uncertainties of the data sets.

The parameters of the initial distributions are given in table 5, and the resulting parton distributions, including the total sea density, $xS(x) = \sum [xq(x) + x\bar{q}(x)]$, are shown at $Q^2 = 4\,\mathrm{GeV}^2$ in figure 10. The inner error band describes the experimental uncertainty, obtained from the criterion $\Delta\chi^2 = 1$ and using the Hessian method as described in [21] and the numerical algorithm presented in [25]. The outer error band represents the experimental and model uncertainties added in quadrature. The latter is obtained by varying:

- the charm mass m_c between $\sqrt{Q_0^2} \simeq 1.38$ GeV and 1.47 GeV,
- the bottom mass m_b between 4.3 and 5.0 GeV,
- the strange fraction f_s from 0.25 to 0.40,
- the value of Q^2_{min}, from 2.25 to $5.0\,\mathrm{GeV}^2$,
- the starting scale of the fit to $Q_0^2 = 1.5\,\mathrm{GeV}^2$.

The implementation of the VFNS scheme prevents the starting scale to be increased beyond the charm mass. Therefore the uncertainty is taken to be symmetric, its value being given by the difference between the nominal fit and what is obtained with $Q_0^2 = 1.5\,\mathrm{GeV}^2$. The model uncertainty at low x is dominated by the sensitivity of the fit on the Q_0^2 choice.

The distributions of $xu_v(x)$, $xd_v(x)$, $xg(x)$ and $xS(x)$ are shown at the starting scale $Q^2 = 1.9\,\mathrm{GeV}^2$ and at $Q^2 = 10\,\mathrm{GeV}^2$ in figures 11a-b and figures 11c-d, respectively, in both linear and logarithmic scales. A comparison of the PDFs at the starting scale with their behaviour in the DIS region, here represented by $Q^2 = 10\,\mathrm{GeV}^2$, illustrates the rather dramatic influence of the DGLAP evolution on the sea and gluon densities. At $Q^2 = 1.9\,\mathrm{GeV}^2$ the sea density rises towards low x in contrast to the gluon distribution, which has a valence quark like behaviour.

P	A	B	C	E
xg	11.60*	0.36	9.41	—
xu_v	5.352*	0.78	4.75	7.41
xd_v	3.227*	0.78*	4.74	—
$x\bar{U}$	0.103*	−0.18	4.00	—
$x\bar{D}$	0.154	−0.18*	4.51	—

Table 5: *Fitted parameters corresponding to the distributions $xg(x)$, $xu_v(x)$, $xd_v(x)$, $x\bar{U}(x)$ and $x\bar{D}(x)$ at the starting scale $Q_0^2 = 1.9\,\mathrm{GeV}^2$ (see section 6.2). The symbol * indicates that the corresponding parameter is not an input parameter of the fit, but is derived from the other parameters.*

The Q^2 evolution rapidly changes the low-x behaviour of the gluon distribution[3], which starts to rise similar as the sea distribution towards low x. In contrast, the non-singlet valence quark distributions evolve very slowly, as expected. As is shown in figures 11c-d, xg is the dominating parton distribution at low x.

The parton distributions determined here may be used for predictions of cross sections at the Tevatron and the LHC.

7 Summary

A new measurement is presented of the inclusive double differential cross section for deep inelastic positron-proton scattering, $e^+p \to e^+X$, in the region of small Bjorken x and medium four-momentum transfer squared, $12\ \mathrm{GeV}^2 \leq Q^2 \leq 150\ \mathrm{GeV}^2$. The data, corresponding to an integrated luminosity of about $22\,\mathrm{pb}^{-1}$, were obtained with the H1 detector at the ep collider HERA at beam energies $E_e = 27.6\,\mathrm{GeV}$ and $E_p = 920\,\mathrm{GeV}$.

The measurement is performed in a wide range of inelasticity y, from 0.005 to 0.6, and of Bjorken x, $2 \cdot 10^{-4} \leq x \leq 0.1$. A small bias in the previously published data set, taken at $E_p = 820\,\mathrm{GeV}$, was found and corrected. The two data sets are then combined and represent the most precise measurement in this kinematic range to date.

The reduced cross section is governed by two independent proton structure functions, F_2 and F_L. The influence of the longitudinal structure function F_L is small in the domain considered here and thus the data are an almost direct measurement of the proton structure function $F_2(x, Q^2)$ and of its derivatives as presented here.

[3] If one chooses a larger starting scale $Q_0^2 = 4\,\mathrm{GeV}^2$, in the "massless" scheme, the description of the data may be improved by adding a linear D_g term in the initial gluon distribution (see equation 4). In this case, two solutions are found by the minimisation procedure. One solution, with D_g consistent with zero, is very similar to what is obtained using a lower starting scale. In the other solution, where the fitted D_g parameter is large, the gluon density at $Q^2 = 4\,\mathrm{GeV}^2$ shows an inflexion point at $x \sim 10^{-3}$, as was observed in [6]. The backward evolution of this solution from $4\,\mathrm{GeV}^2$ to $1.9\,\mathrm{GeV}^2$ and below leads to gluon densities which strongly rise towards low x, developing a marked minimum (maximum) at $x \sim 10^{-3}$ (a few 10^{-2}). In a "massless fit" with $Q_0^2 = 4\,\mathrm{GeV}^2$, the solution with large D_g parameter has as slightly better χ^2.

With this measurement the final data of H1 on the neutral and charged current cross sections from the HERA-I data taking period are available. An NLO QCD fit, using a variable flavour treatment of heavy quark effects, is performed which is able to describe the data very well. This allows a new determination of the gluon and quark densities of the proton. With a reduced uncertainty and more accurate data sets the new H1PDF-HERA-I fit supersedes the H1 PDF 2000 fit previously obtained.

Acknowledgements

We are grateful to the HERA machine group whose outstanding efforts have made this experiment possible. We thank the engineers and technicians for their work in constructing and maintaining the H1 detector, our funding agencies for financial support, the DESY technical staff for continual assistance and the DESY directorate for support and for the hospitality which they extend to the non DESY members of the collaboration. We thank R. Thorne for useful discussions and for providing us with the code to calculate the structure functions in the variable flavour number scheme.

References

[1] C. Adloff *et al.* [H1], *Deep-Inelastic Inclusive ep Scattering at Low x and a Determination of α_s*, Eur. Phys. J. C **21**, 33 (2001), hep-ex/0012053.

[2] S. Chekanov *et al.* [ZEUS], *Measurement of the neutral current cross section and F_2 structure function for deep inelastic e^+p scattering at HERA*, Eur. Phys. J. C **21**, 443 (2001), hep-ex/0105090.

[3] F. D. Aaron *et al.* [H1], *Measurement of the Proton Structure Function F_L at Low x*, Phys. Lett. **B665**, 139 (2008), 0805.2809.

[4] C. Adloff *et al.* [H1], *On the rise of the proton structure function F_2 towards low x*, Phys. Lett. **B520**, 183 (2001), hep-ex/0108035.

[5] F. D. Aaron *et al.* [H1], *Measurement of the Inclusive ep Scattering Cross Section at low Q^2 and x at HERA*, Eur. Phys. J. C **xxx**, xxx (2008), to be published very soon, hep-ex/xxx.

[6] C. Adloff *et al.* [H1], *Measurement and QCD analysis of neutral and charged current cross sections at HERA*, Eur. Phys. J. C **30**, 1 (2003), hep-ex/0304003.

[7] I. Abt *et al.* [H1], *The H1 detector at HERA*, Nucl. Instr. and Meth. A **386**, 310 (1997).

[8] I. Abt *et al.* [H1], *The Tracking, calorimeter and muon detectors of the H1 experiment at HERA*, Nucl. Instr. and Meth. A **386**, 348 (1997).

[9] A. Courau and P. Kessler, *QED Compton scattering in high-energy electron - proton collisions*, Phys. Rev. **D46**, 117 (1992).

[10] A. Kwiatkowski, H. Spiesberger, and H.-J. Moehring, Comp. Phys. Comm. **69**, 155 (1992).

[11] A. Arbuzov *et al.*, Comp. Phys. Comm. **94**, 128 (1996).

[12] J. Kretzschmar, *A Precision Measurement of the Proton Structure Function F_2 with the H1 Experiment*, Doctoral thesis, Humboldt-Universität zu Berlin (2008).

[13] S. Glazov, in *DEEP INELASTIC SCATTERING: 13th International Workshop on Deep Inelastic Scattering; DIS 2005*, edited by W. Smith and S. R. Dasu (AIP Conference Proceedings, 2005).

[14] I. Abt *et al.* [H1], *Measurement of the Proton Structure Function $F_2(x, Q^2)$ in the low x Region at HERA*, Nucl. Phys. B **407**, 515 (1993).

[15] P. W. Johnson and W.-k. Tung, *Precise Treatment of Operator Mixing in Application of Asymptotically Free Theories to Deep Inelastic Scattering*, Phys. Rev. **D16**, 2769 (1977).

[16] C. Adloff *et al.* [H1], *Measurement of neutral and charged current cross-sections in positron proton collisions at large momentum transfer*, Eur. Phys. J. **C13**, 609 (2000), hep-ex/9908059.

[17] C. Adloff *et al.* [H1], *Measurement of neutral and charged current cross sections in electron proton collisions at high Q^2*, Eur. Phys. J. **C19**, 269 (2001), hep-ex/0012052.

[18] R. S. Thorne, *A variable-flavour number scheme for NNLO*, Phys. Rev. **D73**, 054019 (2006), hep-ph/0601245.

[19] M. Botje, QCDNUM version 17β, available at http://www.nikhef.nl/ h24/qcdcode/index.html.

[20] R. Thorne, Fortran code, private communication.

[21] J. Pumplin *et al.*, *New generation of parton distributions with uncertainties from global QCD analysis*, JHEP **07**, 012 (2002), hep-ph/0201195.

[22] C. Pascaud and F. Zomer, preprint LAL-95-05.

[23] R. Thorne, private communication.

[24] C. Amsler *et al.* [Particle Data Group], *Review of particle physics*, Phys. Lett. **B667**, 1 (2008).

[25] J. Pumplin, D. R. Stump, and W. K. Tung, *Multivariate fitting and the error matrix in global analysis of data*, Phys. Rev. **D65**, 014011 (2002), hep-ph/0008191.

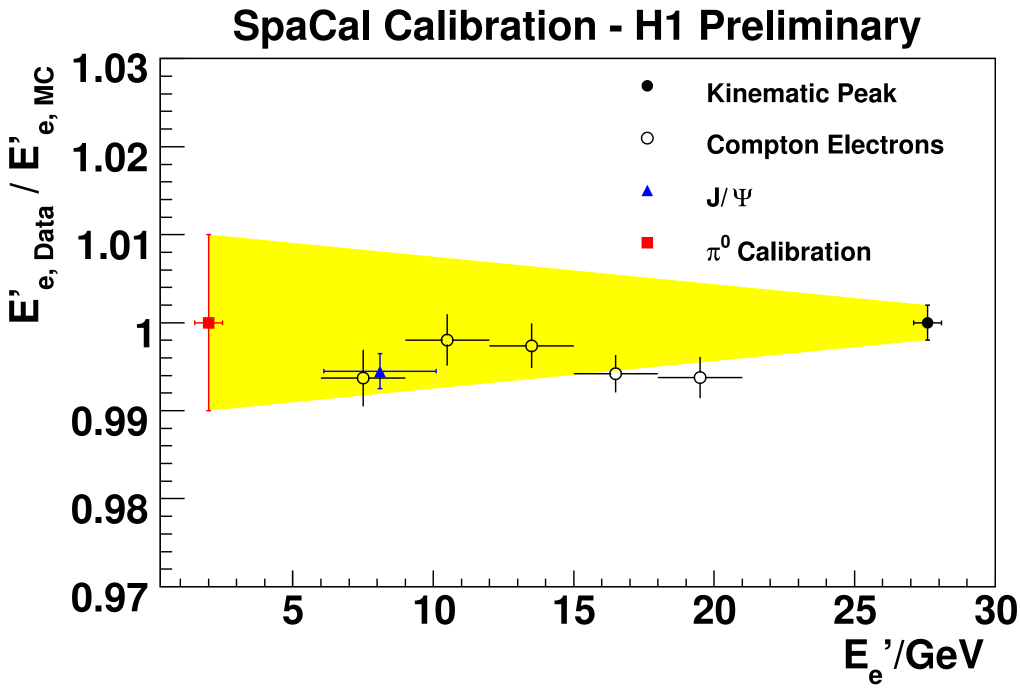

Figure 1: *Summary of SpaCal energy scale determination. The band indicates the uncertainty due to the scale difference between data and the simulation.*

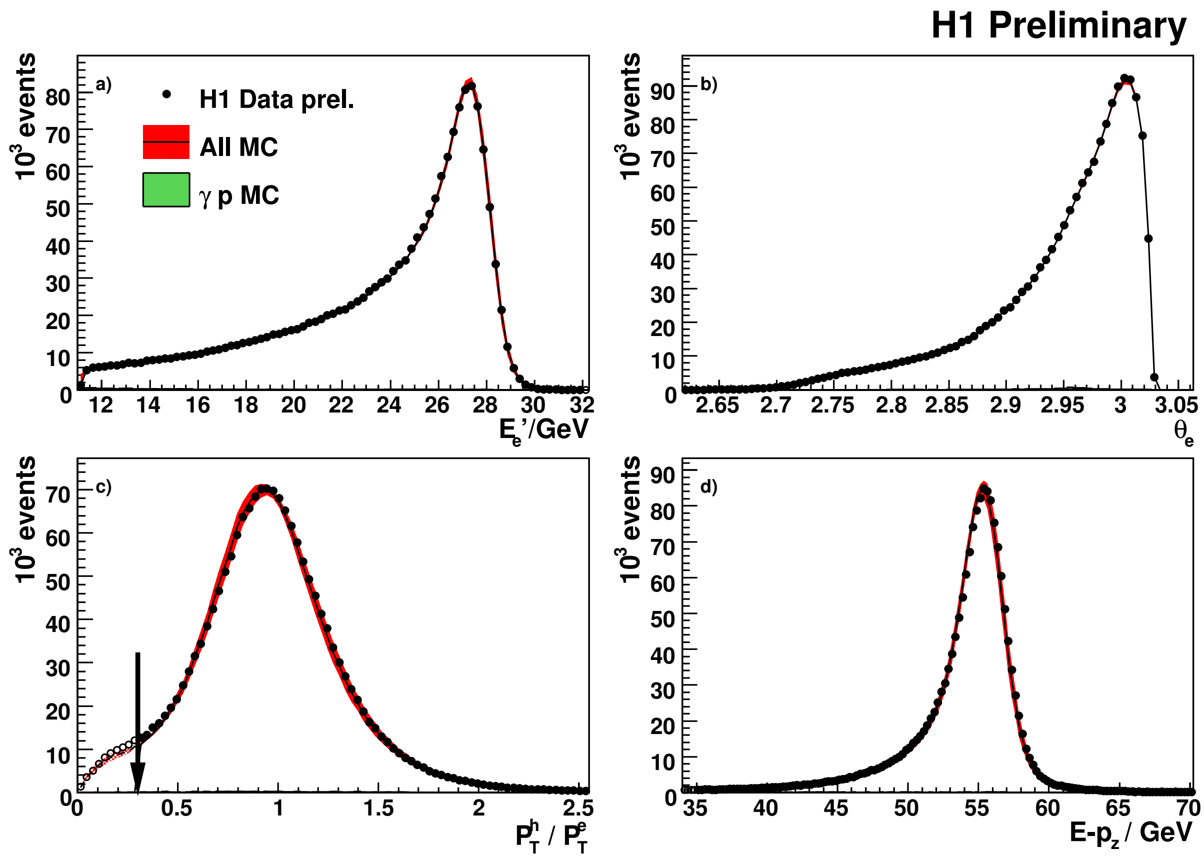

Figure 2: *Distribution of events requiring $y_e < 0.6$ and $y_\Sigma > 0.005$: the energy (a) and the polar angle (b) of the scattered positron, the transverse momentum ratio $P_{\mathrm{T}}^h/P_{\mathrm{T}}^e$ (c) and $E - P_z$ (d). The curves represent the simulation of the measurement normalised to the luminosity and adjusted for a small overall normalisation shift introduced by the cross section averaging procedure and by the QCD fit. The bands illustrate the systematic uncertainty of the measurement. The small photoproduction background is drawn green (shaded).*

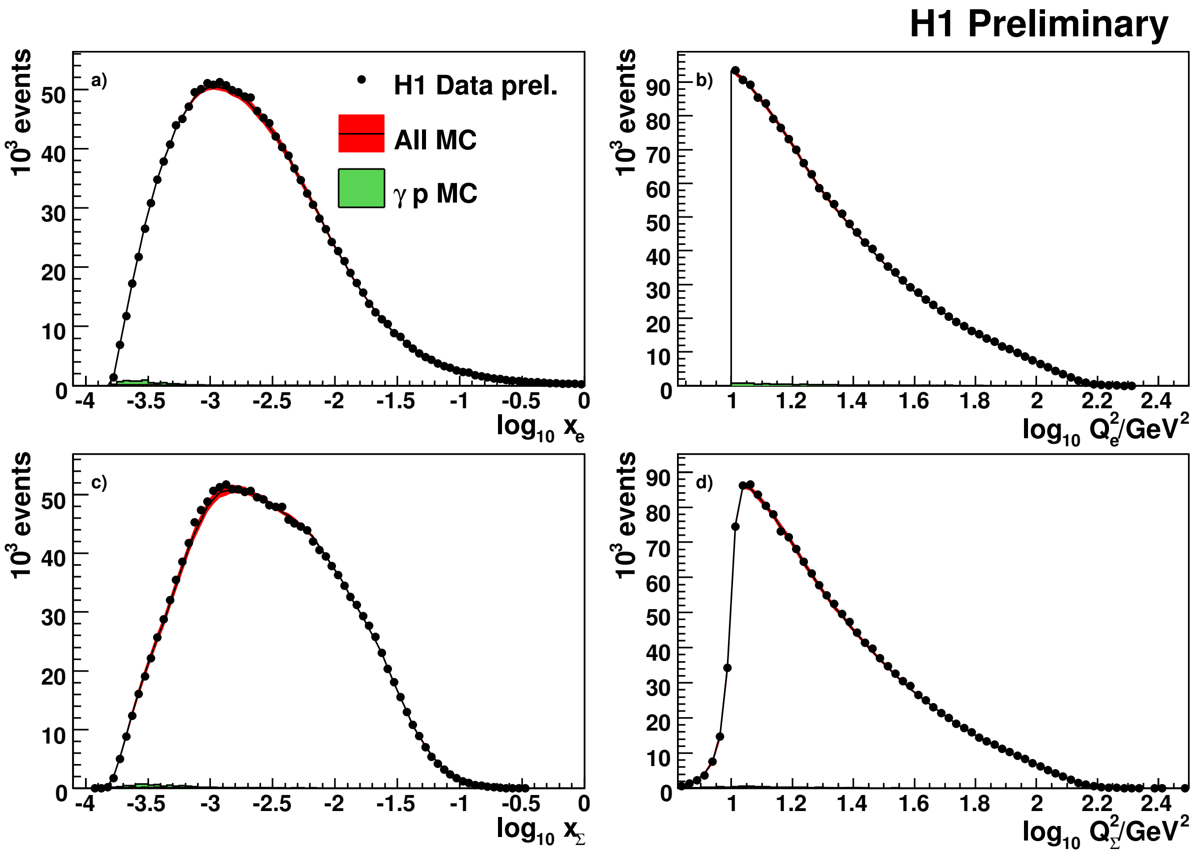

Figure 3: *Distribution of events requiring $y_e < 0.6$ and $y_\Sigma > 0.005$: the Bjorken-x (a,c) and Q^2 (b,d) using the electron (Σ) method. The curves represent the simulation of the measurement normalised to the luminosity and adjusted for a small overall normalisation shift introduced by the cross section averaging procedure and by the QCD fit. The bands illustrate the systematic uncertainty of the measurement. The small photoproduction background is drawn green (shaded).*

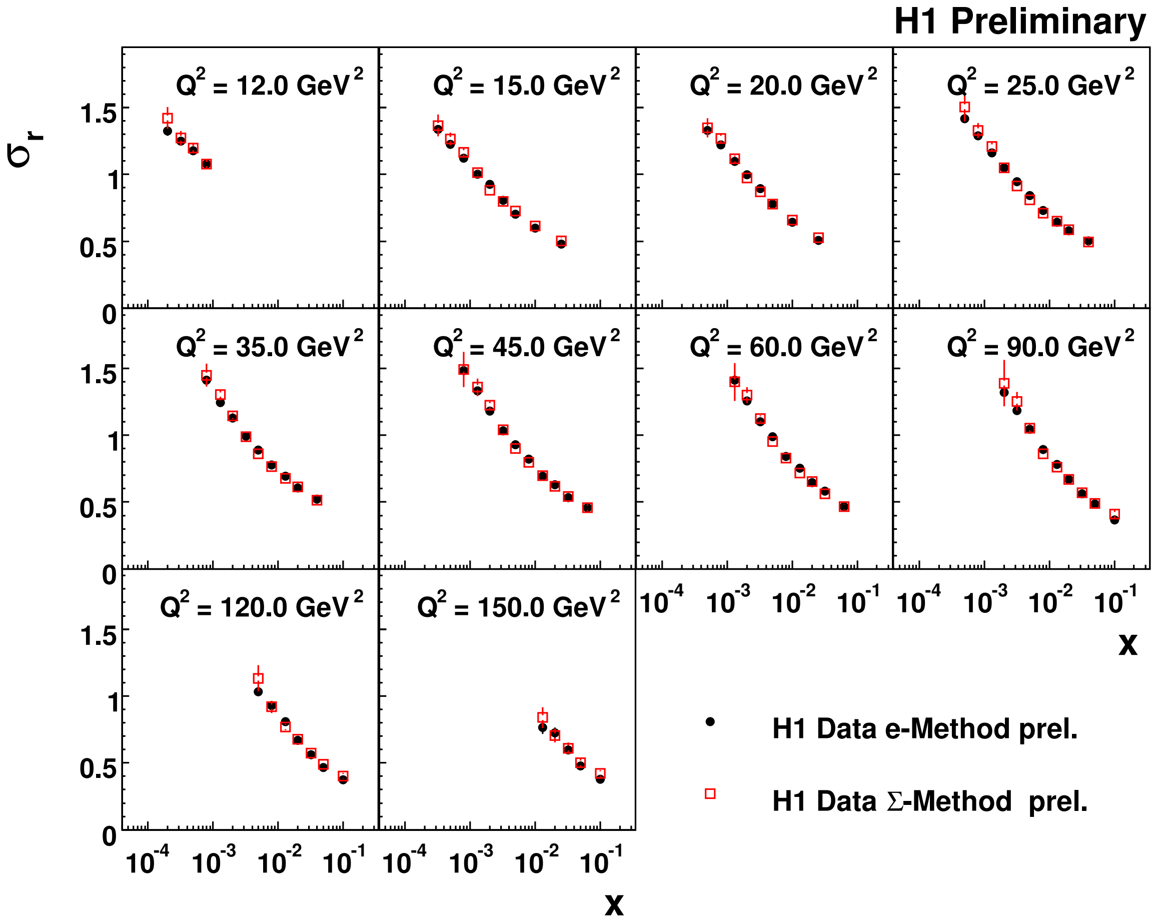

Figure 4: *Comparison of reduced cross sections as obtained with the electron (closed circles) and Σ (open squares) reconstruction methods. The error bars represent the total measurement uncertainties.*

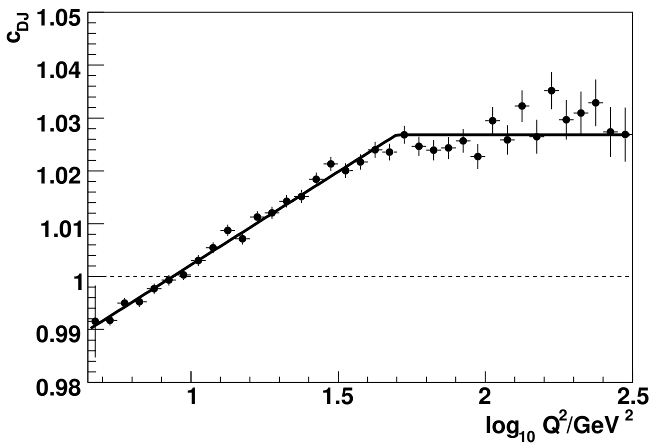

Figure 5: *Correction factor applied to the published DIS cross section data from [1], see text.*

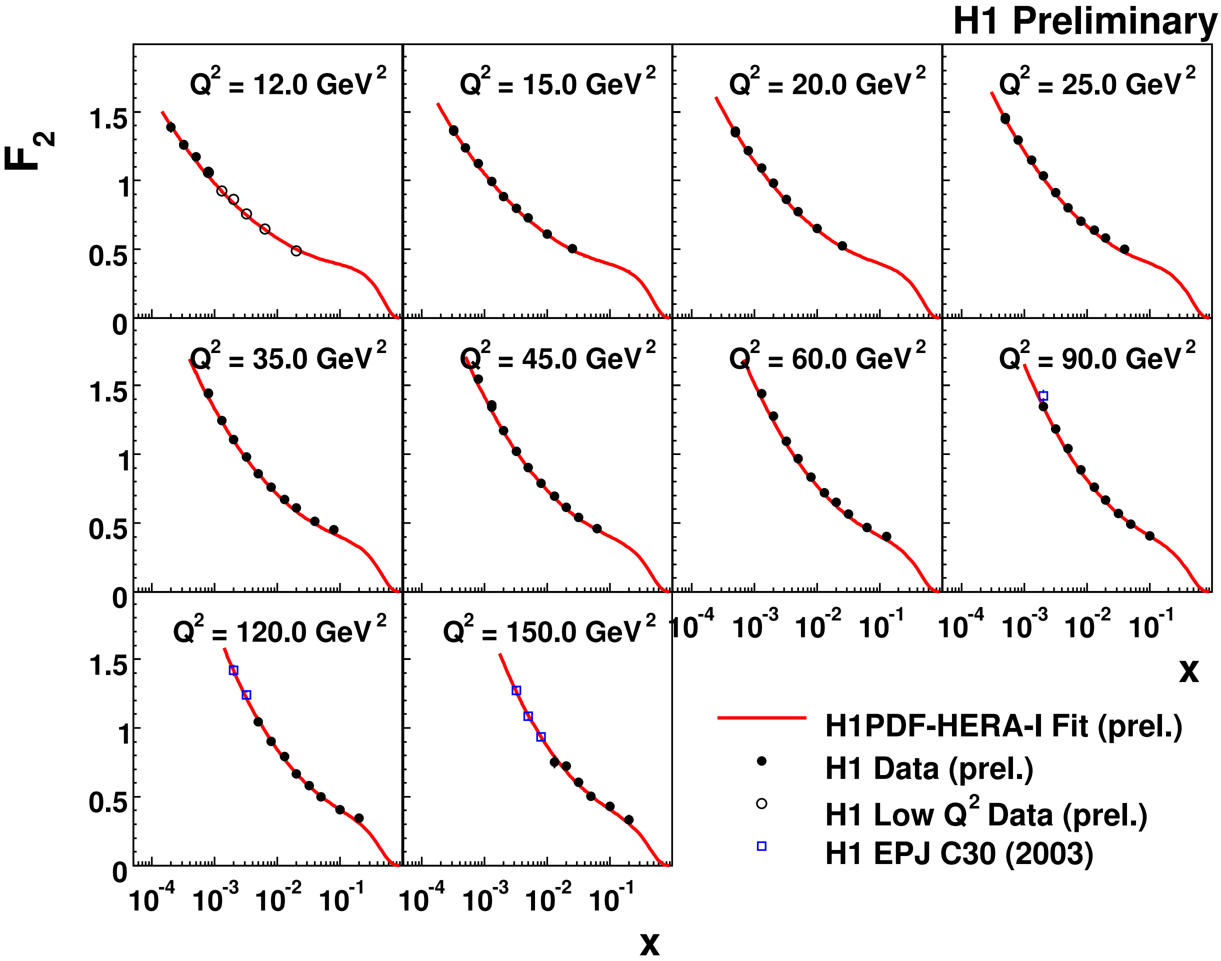

Figure 6: *Comparison of this measurement of F_2 (solid, black circles) with the published data at high Q^2 (open boxes) and low Q^2 (open circles). The error bars represent the total measurement uncertainties. The curve represents the QCD fit described in this paper.*

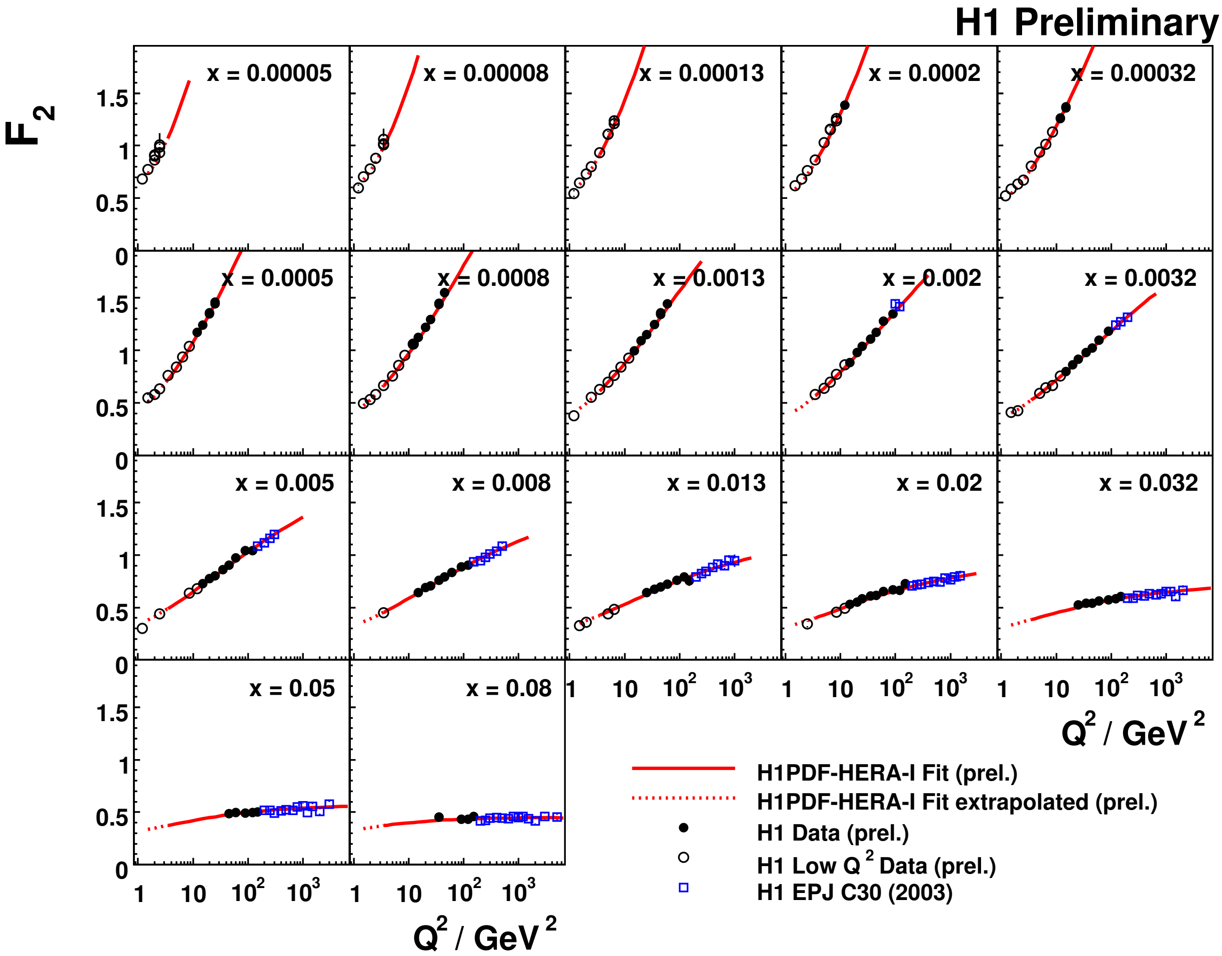

Figure 7: *Measurement of the electromagnetic proton structure function F_2 corrected for electroweak effects as a function of Q^2 at various values of x. The data of this measurement (solid, black circles) is complemented with the published data at high Q^2 (open boxes) and low Q^2 (open circles). The error bars represent the total measurement uncertainties.*

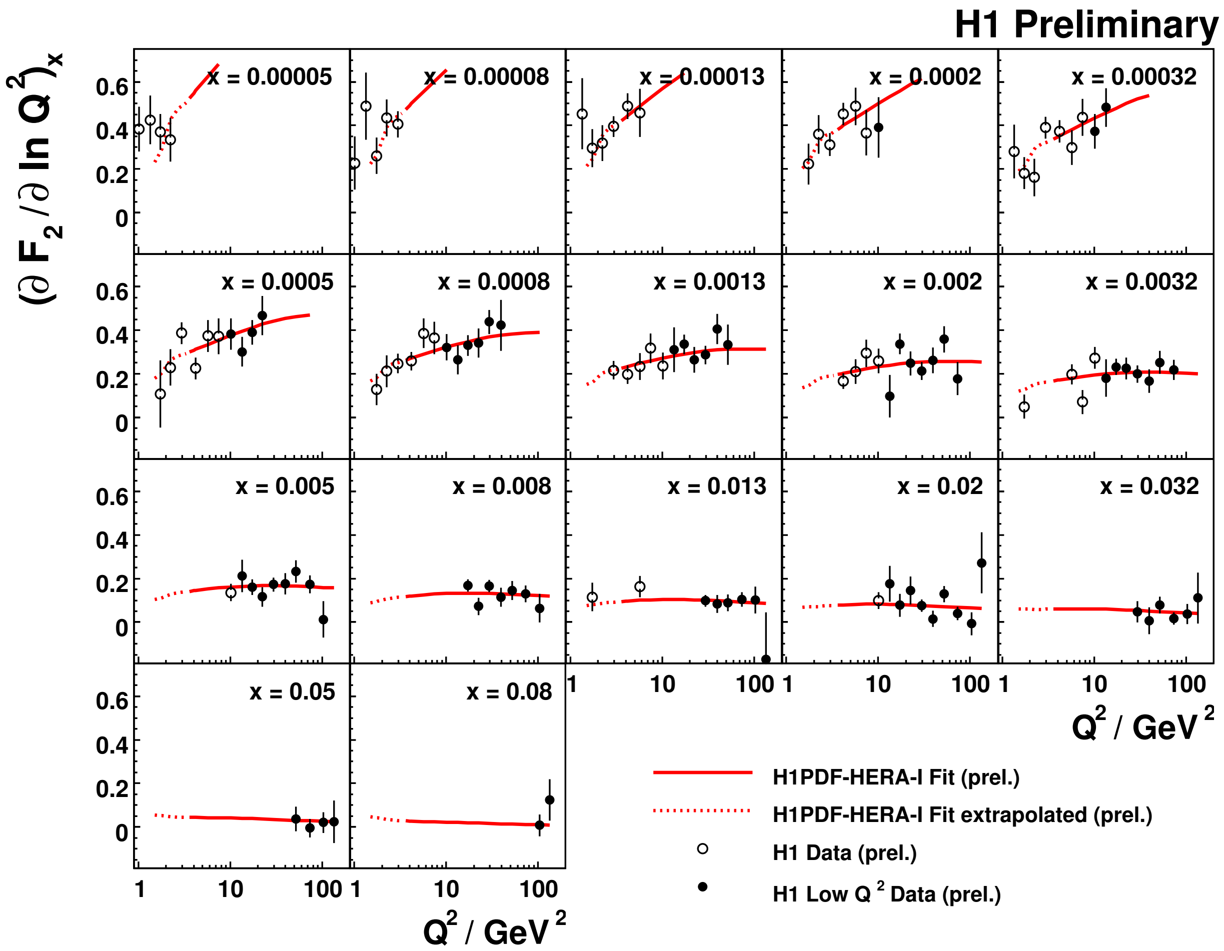

Figure 8: *Logarithmic derivative of the proton structure function F_2 as a function of Q^2 at various values of x. The data of this measurement (solid, black circles) is complemented with the published data at lower Q^2 (open circles). The error bars represent the total measurement uncertainties.*

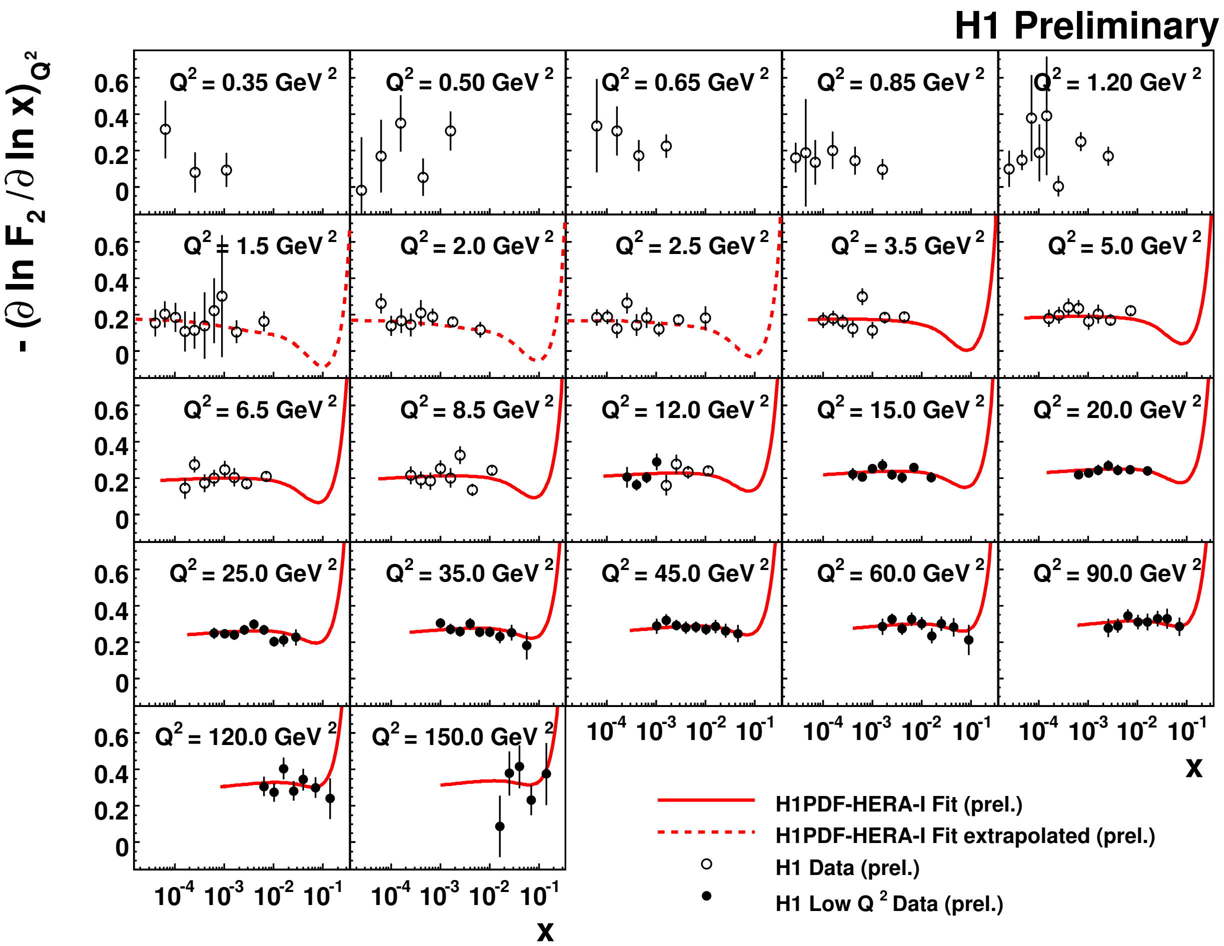

Figure 9: *Measurement of the function $\lambda(x, Q^2)$, defined as the negative logarithmic derivative of $\ln F_2$ as a function of x at various values of Q^2. The data of this measurement (solid, black circles) is complemented with the published data at lower Q^2 (open circles). The error bars represent the total measurement uncertainties.*

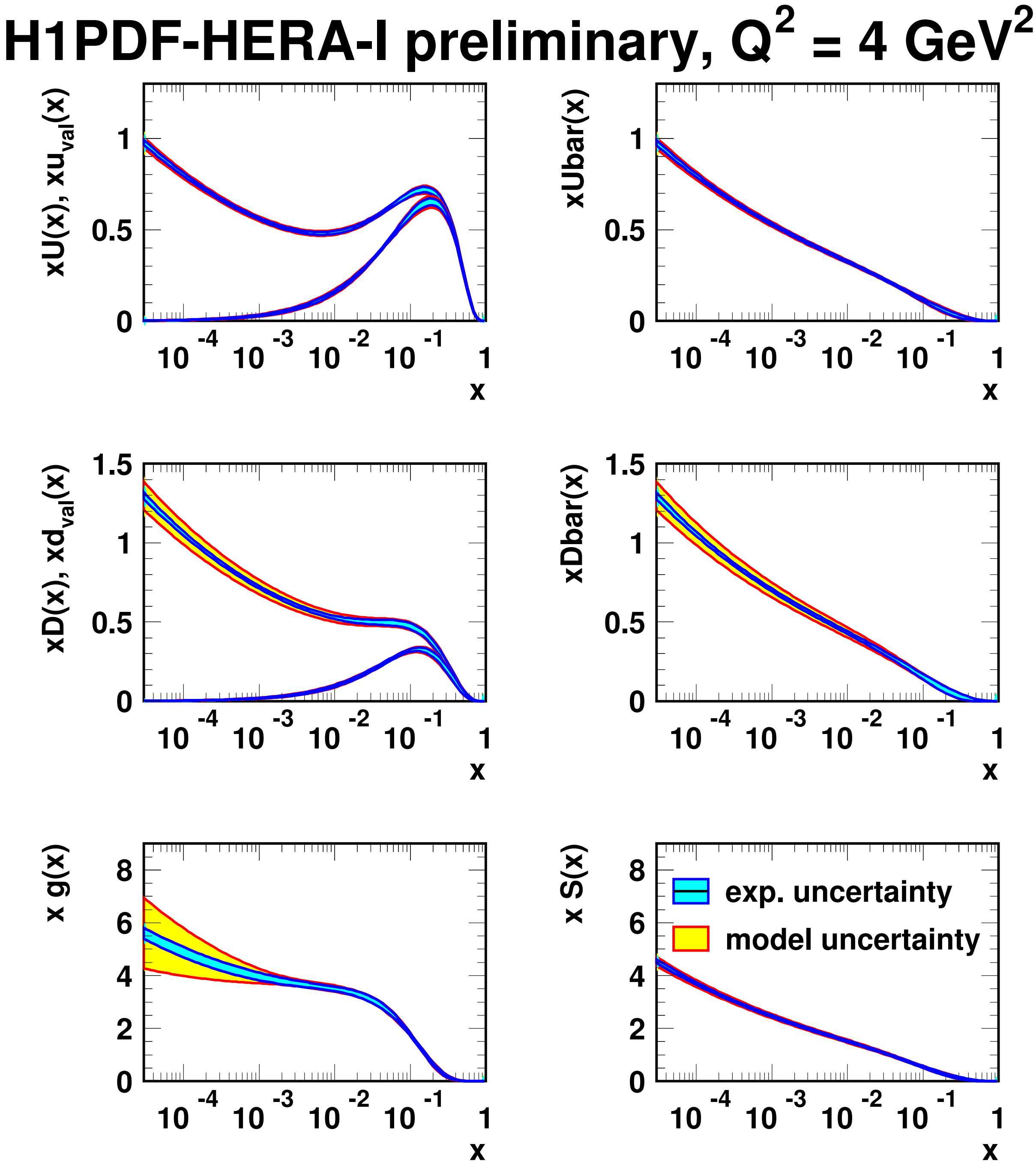

Figure 10: *Parton distributions as determined by the H1PDF-HERA-I QCD fit at $Q^2 = 4$ GeV^2. The inner error bands show the experimental uncertainty and the outer bands correspond to the total uncertainty, including the uncertainties of the fit assumptions.*

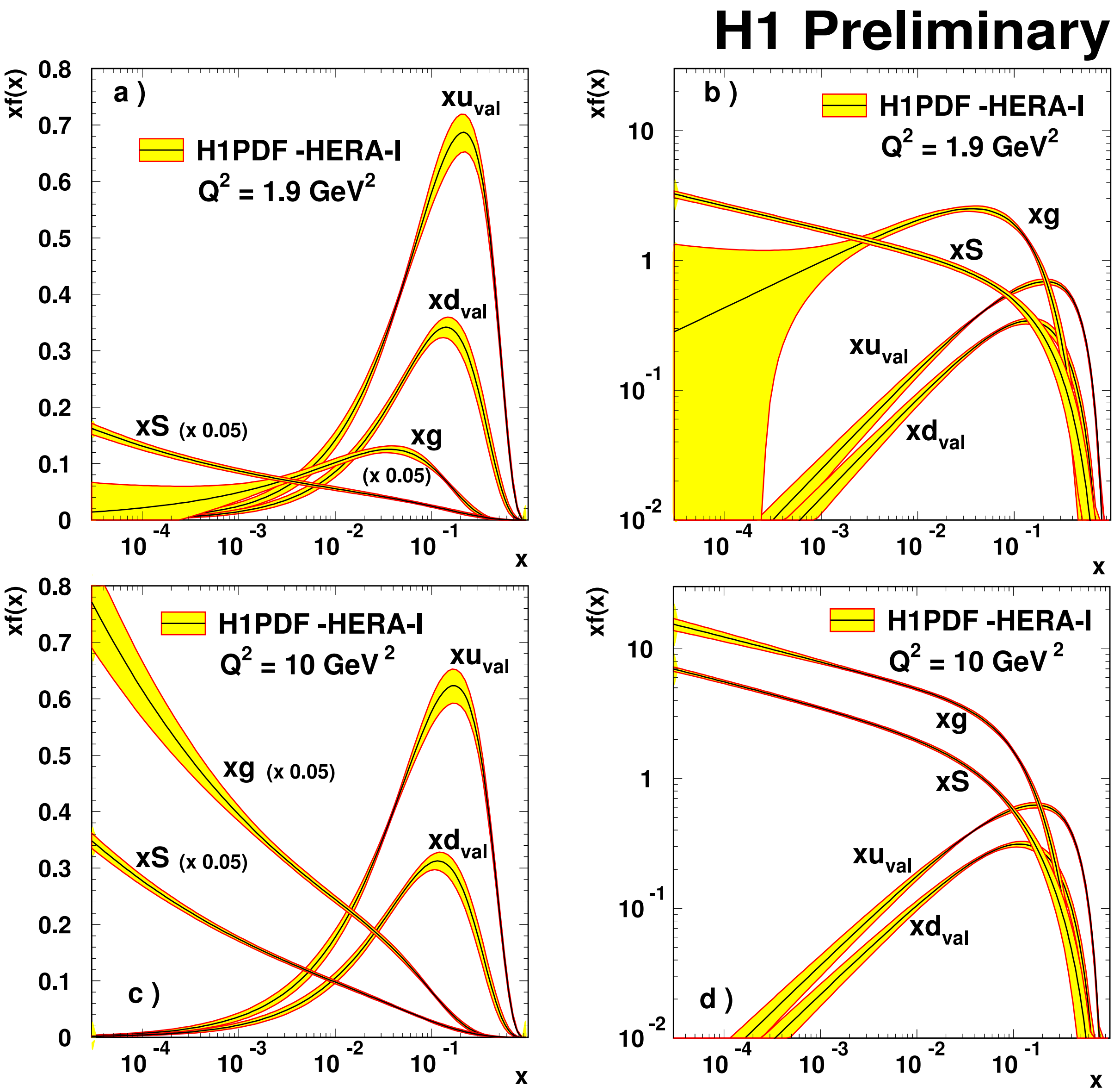

Figure 11: *Parton distributions as determined by the H1PDF-HERA-I QCD fit at Q^2 = 1.9 GeV^2 (a-b) and at Q^2 = 10 GeV^2 (c-d). In a and c (linear vertical scale), the gluon and sea densities are downscaled by a factor 0.05. The uncertainty corresponds to the quadratic sum of the experimental and model uncertainties.*